Check for updates

A solar/radiative cooling dual-regulation smart window based on shape-morphing kirigami structures†

Shancheng Wang, [ID] ‡[ab] Yuting Dong,‡[b] Yanbin Li,‡[c] Keunhyuk Ryu,[b] Zhili Dong,[b] Jian Chen,[d] Zhendong Dai,[d] Yujie Ke,*[e] Jie Yin*[c] and Yi Long [ID] *[af]

The energy efficiency of buildings has become a critical issue due to their substantial contribution to global energy consumption. Windows, in particular, are often the least efficient component of the building envelope, and conventional smart windows focus solely on regulating solar transmittance while overlooking radiative cooling. Although several recent designs achieved dual-control of solar and radiative cooling, these windows still face limitations in terms of durability, limited modulation ability and energy-saving performance. To address these challenges, we propose a novel dual-control smart window design consisting of a reconfigurable kirigami structure and polydimethylsiloxane-laminated thermochromic hydrogel coated with silver nanowires. In summer, the thermochromic hydrogel turns translucent to suppress the solar heat gain, while the high emissivity kirigami structure covers the exterior surface of the window, promoting radiative cooling. In winter, the hydrogel becomes transparent to allow for solar transmission. Additionally, the kirigami structure undergoes an out-of-plane structural change, opening towards the outside environment to expose the underlying low-emissivity silver nanowires and suppress heat radiation. Our design achieves a promising solar transmittance modulation ability of ∼24% and a good long-wave infrared emissivity regulation ability of

New concepts

We propose a novel design of a solar transmittance/radiative cooling dual-control smart window, inspired by the ancient Asian art of kirigami. Existing solar transmittance/radiative cooling dual-controlling windows suffer from limited durability and energy-saving performance; however, our design shows a prolonged lifetime at both room temperature and high temperature with enhanced energy-saving performance. Such enhancements are achieved by combining a shape-morphing kirigami structure with a silver nanowire-coated polydimethylsiloxane (PDMS) laminated thermochromic hydrogel. We demonstrate that the laminated hydrogel has a lifespan that is nine times longer than that of conventional smart hydrogels, while still maintaining a promising solar modulation ability. Meanwhile, the stretching-induced out-of-plane shape morphing in the kirigami structure exposes the underlying silver nanowires. By controlling the opening and closing of the kirigami structure, the long-wave infrared emissivity of the window can be regulated with a modulation ability of 0.5. The new design offers a good solar and radiative cooling regulation ability, leading to an improved average energy-saving performance compared to state-of-the-art dual-control window designs, which paves the way for the development of new smart window technologies with improved efficiency and durability.

0.5. Furthermore, it exhibits significantly improved durability, which is nine times longer than the lifespan of conventional smart hydrogels. Our novel approach offers a promising solution for constructing energy-efficient and durable smart windows and outperforms existing state-of-the-art solar/radiative cooling dual-regulation smart windows in the literature.

Introduction

Buildings are responsible for approximately half of the global electricity supply,[1] and windows are among the least energy-efficient components of building envelopes.[2,3] In the United States, window-associated heating and cooling energy consumes about 4% of the national primary energy usage.[4] To address this issue, researchers have developed several types of chromogenic

[a] *Department of Electrical Engineering, The Chinese University of Hong Kong, Shatin, New Territories, Hong Kong SAR, China. E-mail: yilong@cuhk.edu.hk*

[b] *School of Materials Science and Engineering, Nanyang Technological University, 639798, Singapore*

[c] *Department of Mechanical and Aerospace Engineering, North Carolina State University, Raleigh, North Carolina 27695, USA. E-mail: jyin8@ncsu.edu*

[d] *Jiangsu Provincial Key Laboratory of Bionic Functional Materials, College of Mechanical and Electrical Engineering, Nanjing University of Aeronautics and Astronautics, Nanjing 210016, China*

[e] *Institute of Materials Research and Engineering (IMRE), Agency for Science, Technology and Research (A*STAR), 2 Fusionopolis Way, Innovis #08-03, Singapore 138634, Republic of Singapore. E-mail: yujie_ke@imre.a-star.edu.sg*

[f] *Institute of Environment, Energy and Sustainability (IEES), The Chinese University of Hong Kong, Shatin, New Territories, Hong Kong SAR, China*

† Electronic supplementary information (ESI) available. See DOI: https://doi.org/10.1039/d3mh00671a

‡ These authors contributed equally to this work.

smart windows such as electro-[5,6] thermo-,[7,8] photo-,[9,10] and mechano-chromic windows[11,12] to improve the energy efficiency of windows by regulating the visible (360–780 nm) and near-infrared (NIR, 780–2500 nm) transmittance. Although these types of chromogenic smart windows have shown promise in improving energy efficiency, they can only regulate solar radiation while generally overlooking the broadband infrared emissivity ($\varepsilon_{Broadband}$, 2.5–25 μm) and its accompanied radiative cooling (RC) effect. RC is a technique that spontaneously cools an object through emitting strong thermal radiation towards the sky and minimizing solar radiation absorption.[13,14] Recent reports have demonstrated that an ideal energy-efficient smart window should have a low solar transmittance (T_{sol}, 250–2500 nm) and a high $\varepsilon_{Broadband}$ in the summer to minimize solar radiation absorption and maximize the RC, respectively; while the window in winter should have a high T_{sol} to promote solar heating and a low $\varepsilon_{Broadband}$ to suppress RC.[15]

Based on the aforementioned state-of-the-art design principle, several dual-control smart windows have been recently developed by employing a thermal-responsive material to construct optical modulation structures,[15,16] thermal-responsive water capture/release in a hydrogel,[17] reversible electrodeposition of a metal,[18] reversible crack creation on a low-E film,[19] and mechanical flipping between high-/low-E faces.[20] These designs can spontaneously control the solar transmittance while regulating the RC power. Consequently, these dual-control smart windows offer significantly improved energy efficiency compared to conventional smart windows, particularly in regions with four distinct seasons.

Despite the promise of these dual-control smart window designs, they still face limitations in terms of durability and modulation capability. For example, the thermal-responsive vanadium dioxide (VO_2) is prone to oxidation[21,22] and although existing remedies such as sealing[23,24] and encapsulation[25] can improve the durability of VO_2, this is at the cost of

defunctionalizing VO_2's $\varepsilon_{Broadband}$ modulation ability. Stimuli-responsive hydrogels and reversible metal electrodeposition also suffer from durability issues due to factors such as vulnerability to drying[26,27] and electrochemical cell performance degradation.[28,29] Meanwhile, the reversible crack creation approach has limited RC regulating performance[19] and the facile mechanical flipping technique requires specially designed pivoted window frames and manual operation to achieve high regulating performances.[20] Therefore, a solar/RC dual-control smart window with both good durability and promising solar/RC regulating performance is highly desired.

To address these issues, we have developed a new design of a kirigami-inspired durable solar/RC dual-control smart window by integrating thermal-responsive hydrogels with an out-of-plane reconfigurable kirigami structure. As shown in Fig. 1(a) and (b), the design consists of two components: (1) polydimethylsiloxane (PDMS) laminated thermal-responsive composite hydrogels coated with AgNWs based on physical-crosslinked poly(N-isopropylacrylamide) (PNIPAm) and acrylamide and (2) a PDMS-based kirigami structure with strain-responsive out-of-plane opening for emissivity tuning. Its working principles in summer and winter are illustrated in Fig. 1(c) and (d), respectively. In summer, the high-E PDMS kirigami is in the released state to cover the entire exterior surface of the window to enhance RC, while the hydrogel composite becomes translucent to suppress solar transmission when the ambient temperature surpasses its lower critical solution temperature (LCST, 20 °C for the thermal-responsive composite hydrogel). In winter, the kirigami structure undergoes out-of-plane structural change and opens towards the outside environment to expose the underlying low-E AgNWs layer to suppress RC, while the smart hydrogel becomes transparent to allow for solar transmission and heating. The transparent-to-translucent transition of the hydrogel is based on a phase separation process due to the hydrophobic-to-hydrophilic changes of the PINIPAm polymer across its LCST.[30,31] The newly designed smart window has a lifetime nine times longer than those of conventional smart hydrogels and it exhibits a promising $\varepsilon_{Broadband}$ regulation ability ($\Delta\varepsilon_{Broadband}$) of 0.5 ($\varepsilon_{Broadband, Release}$: 0.95, $\varepsilon_{Broadband, Stretch}$: 0.45). Due to its balanced luminous transmittance (T_{lum}, 360–780 nm), solar modulation ability (ΔT_{sol}, 250–2500 nm), and $\Delta\varepsilon_{Broadband}$, the new design outperforms the literature-reported designs of state-of-the-art solar/radiative cooling dual-regulation smart windows regarding the global energy-saving performance. Our new design of a durable solar/RC dual-control smart window provides a new strategy to pave the way for real-world applications.

Characterization of the PNIPAm-based hydrogel and AgNWs coating

As PNIPAm is the active ingredient that fulfils the functionality of solar transmittance regulation in the hydrogel composite, we investigated the thermochromic property changes in terms of the PNIPAm concentration in the hydrogel composite (Fig. S1 and Table S1, ESI†) and summarized the results in Fig. 2(a). All the hydrogel composites show a similar $T_{lum,15\,°C}$ of
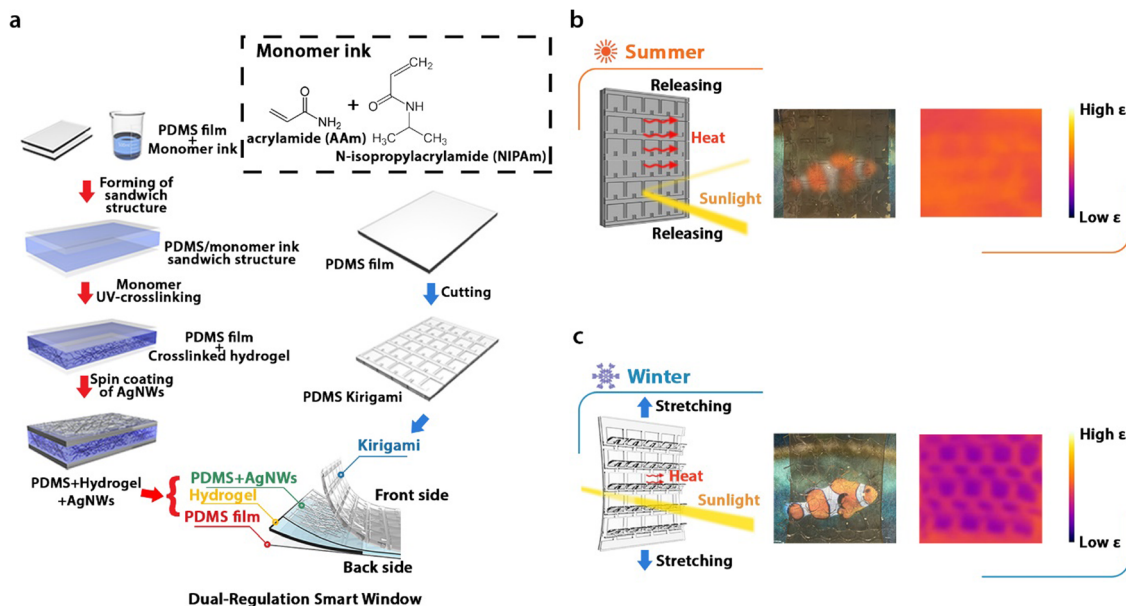
Fig. 1 (a) The formula of acrylamide and *N*-isopropylacrylamide monomers used in smart monomer ink and schematics of the fabrication process and structure of the durable solar/RC dual-control smart window. (b) The working principle of the durable solar/RC dual-control smart window in summer and its corresponding photo and IR camera image. The red arrows represent thermal radiation and the yellow line represents sunlight. In summer, the high-E kirigami overlayer closes to promote thermal radiation and the hydrogel turns translucent to block the sunlight. (c) The working principle of the durable solar/RC dual-control smart window in winter and its corresponding photo and IR camera image. In winter, the kirigami overlayer opens towards the outside environment under in-plane stretching, which allows sunlight to enter the room to suppress the RC to minimize heat loss.

~90%, irrespective of their PNIPAm concentration, while their ΔT_{sol} increases when the PNIPAm concentration was increased from 5 wt% to 10 wt% and reached a plateau at approximately 60% for samples with a PNIPAm concentration above 10 wt%. All the smart hydrogel samples experience hydrophobic-to-hydrophilic phase transitions in response to a thermal stimulus and show an LCST of 20 °C (Fig. S2, ESI†), which is significantly lower than the pure PNIPAm of 30 °C.[32] Additionally, the viscosity of the monomer ink increased with increasing the NIPAm concentration (5 wt% PNIPAm sample: 115.8 cP; 20 wt% PNIPAm sample: 2650.6 cP) and the monomer ink successfully crosslinked to form hydrogels under UV irradiation, which has been proven by the storage modulus (G') and loss modulus (G'') changes (Fig. S3, ESI†). Meanwhile, Fig. S4 (ESI†) illustrates the stress–strain curve of the crosslinked hydrogel with different PNIPAm concentrations. It can be observed that when the PNIPAm concentration increases from 5 wt% to 20 wt%, the Young's modulus of the hydrogel decreases from 38.08 ± 0.35 kPa to 24.64 ± 0.25 kPa. To balance the thermochromic properties, fabrication quality, and mechanical properties, the hydrogel with 10 wt% PNIPAm was chosen for the application in the durable solar/RC dual-control smart window. Fig. 2(b) shows the UV-Vis-NIR spectra for the composite hydrogels with 10 wt% PNIPAm at 15 °C and 45 °C. The 1 mm thick hydrogel sample has a T_{lum} of 88.8% and a ΔT_{sol} of 60.5% with a transparent appearance at 15 °C and a translucent appearance at 45 °C (Fig. 2(c)). The photos of the hydrogel composites with different PNIPAm concentrations are shown in Fig. S5 (ESI†). The light regulation behaviour of the PNIPAm-based hydrogel composite is attributed to the porous polymer networks as demonstrated by the scanning electron

microscope (SEM) images. At low temperatures, the size of the pores is large, which allows the light to pass through. In contrast, the pores shrink when heated and serve as scattering centres, resulting in a decrease in transmittance.

Meanwhile, we tested and calculated the T_{lum}, T_{sol}, and $\varepsilon_{Broadband}$ for the PDMS films with different layers of coatings of AgNWs (Fig. 2(d), Fig. S6, S7 and Table S2, ESI†). The transparency of the PDMS films with varying layers of coatings of AgNWs is shown in Fig. S8 (ESI†) and the $\varepsilon_{Broadband}$ of the coated PDMS films decreases from 0.70 to 0.16 with increasing the coating layers from 1 to 15, which is consistent with their IR photos (Fig. S9, ESI†). The T_{lum} and T_{sol} follow a similar trend to the $\varepsilon_{Broadband}$. Since $\Delta\varepsilon_{Broadband}$ is crucial for energy saving, an optimal 15-layer AgNWs coating on PDMS film was chosen for application in the durable solar/RC dual-control smart window. The $\varepsilon_{Broadband}$ of the stretched AgNWs coated PDMS is lower (0.16) than that of the released state (0.34) throughout the wavelength range of 2.5–20 μm, as shown in Fig. 2(e). This behaviour can be attributed to the surface roughness change induced by the stretch/release of the PDMS substrate (Fig. 2(f)). As the PDMS substrate is pre-stretched to 40% strain during the spin coating process, the AgNWs layers become wrinkled in the released state, leading to increased surface roughness and consequently an increase in $\varepsilon_{Broadband}$. In contrast, the surface of the AgNWs layer is smooth in the 40% stretched state, causing a lowered $\varepsilon_{Broadband}$.

The design of the kirigami-inspired out-of-plane shape-morphing structures

In contrast to the reported cutting methods used for kirigami structures, which commonly produce in-plane structural
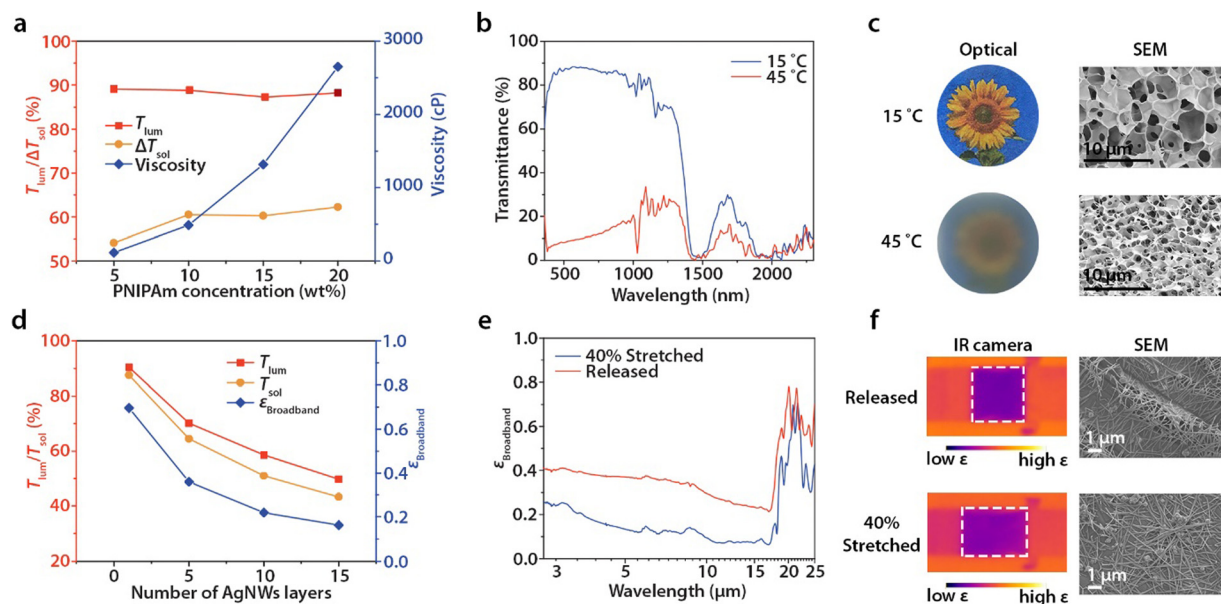
Fig. 2 (a) Thermochromic properties for the hydrogel composite and viscosity of monomer ink with different PNIPAm concentrations. (b) UV-Vis-NIR spectra for 10 wt% PNIPAm hydrogel at 15 °C and 45 °C. (c) The photo and SEM image of the smart hydrogel at 15 and 45 °C. (d) The T_{lum}, T_{sol}, and integrated $\varepsilon_{Broadband}$ for the PDMS film with different layers of coatings of AgNWs. (e) The broadband emissivity spectra of the 15-layer AgNWs-coated PDMS film in its released and 40%-stretched states. (f) IR camera images and SEM images for the 15-layer AgNWs-coated PDMS film in its released and 40%-stretched states.

changes,[33,34] we adapted a kirigami pattern to achieve out-of-plane reconfigurable structural changes[35] and investigated its behaviour with different feature parameters. The geometric designs of the kirigami patterns and their feature parameters are displayed in the upper part of Fig. 3(a) and Fig. S10 (ESI†), respectively. We defined the asymmetric cut ratio as the height ratio between the upper patterns (labelled as H_1 in Fig. 3(a)) and lower patterns (labelled as H_2 in Fig. 3(a)). The photos of the paper kirigami structures with different asymmetric cut ratios are illustrated in the middle part of Fig. 3(a). Under the 40%-stretching state, the sample with an asymmetric ratio of 1 deforms and opens symmetrically on two sides out of the original plane (highlighted with the red dashed line in Fig. 3(a)). Conversely, the sample with a ratio of 3 opens asymmetrically towards one side only. Similar structural change behaviour was observed in the PDMS kirigami structures (Fig. 3(a), lower part, Fig. S11, ESI†).

To quantitatively understand the asymmetrical reconfiguration behaviour of the kirigami structure, we defined two performance indices, namely, length ratio and covering ratio (Fig. 3(b), upper part). Finite element method simulations (FEM) were conducted for the samples with various asymmetric ratios and the results are presented in Fig. 3(b) (middle part). Both the simulation and experiment results suggest that the length ratio increases linearly with the increasing asymmetric ratio (Fig. 3(b), lower part): *i.e.*, kirigami structures with higher asymmetric ratios tend to open towards one side upon stretching with a smaller portion at the other side of the original plane. The one-side opening will minimize the squeezing and scratching of the underlying AgNWs layer during the kirigami structural reconfiguration and extend the lifetime of the

AgNWs. On the other hand, the change in the covering ratio is insignificant regarding the asymmetric ratio changing, indicating that the change of opening direction will not affect the exposure degree of the underlying AgNWs layer and its maximum $\varepsilon_{Broadband}$ regulation ability. The working principle for the directional opening is further investigated by FEM simulations (Fig. S12 and Videos S1–S5, ESI†). The models with different asymmetric ratios from 1 to 10 were stretched and all the structures buckle out of the stretching plane and overlap with a pivot axis at the centre of two adjacent cut slits (Fig, S13, ESI†). Meanwhile, the stress distributions in the kirigami structures with different asymmetric ratios are mapped (Fig. S14, ESI†). The maximum value of the concentrated stress in the kirigami structure is ∼0.00186 MPa, which is significantly lower than the rupture stress threshold of the PDMS materials (∼0.83 MPa).

In the design of kirigami for smart window applications, strength and stiffness are critical factors. The ideal kirigami structure for smart window applications should be responsive to small amounts of tensile stress, which means that it should have low tensile strength and stiffness. We prepared kirigami structures with different PDMS thicknesses (Fig. S15, ESI†) and tested their tensile strength and stiffness. Fig. 3(c) shows the stress–strain curves of kirigami structures with different PDMS thicknesses from 0.3 to 0.6 mm. With the film thickness increasing, the kirigami structures show an increased Young's modulus and toughness (Fig. 3(d)). The opening angle is also affected by the thickness: the 0.3 mm sample exhibits an open angle of 75.5° at a stretched strain of 40%, while the 0.6 mm sample only opens to 44.5° (Fig. 3(e)). Therefore, a PDMS film with a thickness of 0.3 mm is preferred for smart window
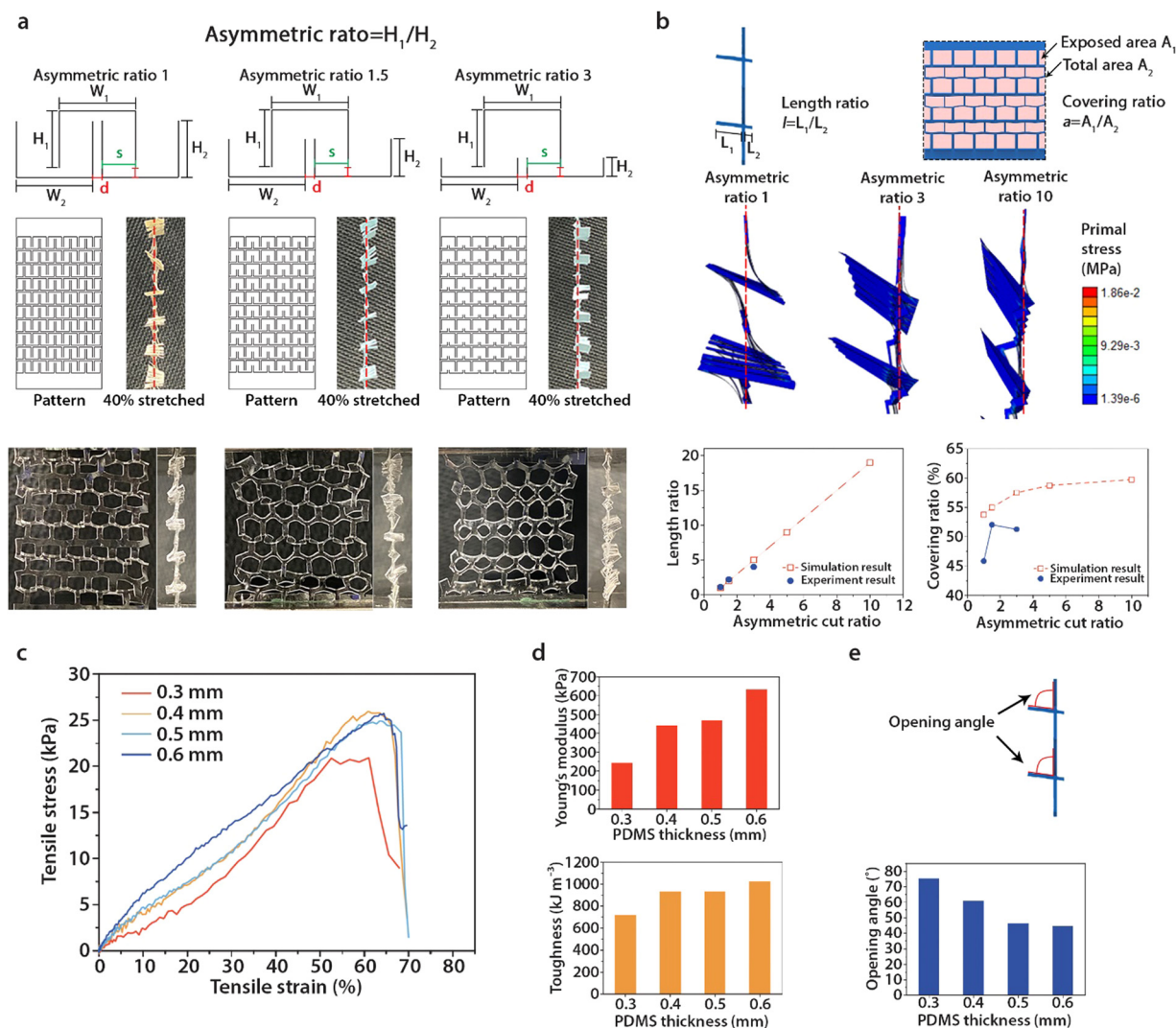
Fig. 3 (a) A schematic of the out-of-plane reconfigurable kirigami pattern with different asymmetric cut ratios (upper part), its corresponding paper kirigami structures under 40% stretching (middle part), and its corresponding PDMS structures under 40% stretching (lower part). The red dashed line indicates their original plane in the released state. (b) Numerical analysis for the out-of-plane structural changes of kirigami structures. Upper part: Schemes of the indexes to describe the out-of-plane structural changes: the length ratio and the covering ratio. Middle part: simulated model for asymmetric ratio 1, 3, and 10 samples. Lower part: experimental (solid dots) and simulated (hollow squares and dashed line) results for the length ratio and covering ratio of samples with different asymmetric ratios. (c) Stress−strain curves for the kirigami structures with different PDMS film thicknesses. (d) The effect of the PDMS thickness on the Young's modulus and toughness. (e) A schematic of the opening angle and the experimental angle analysis for samples with different PDMS thicknesses under 40% stretching.

applications due to its relatively low tensile strength and stiffness, as well as the relatively large opening degree upon stretching. It is worth noting that the 0.3 mm PDMS kirigami structure shows little change in T_{lum} between the released and 40% stretched states (Fig. S16, ESI†), which suggests that the out-of-plane structural change process will not affect its optical properties.

Performance evaluation of the durable solar/RC dual-control smart window

We further evaluated the performance of the fabricated durable solar/RC dual-control smart window. Fig. 4(a) shows the UV-Vis-NIR spectra of the smart window at 15 °C and 45 °C,

respectively. The smart window has a lower T_{lum} and ΔT_{sol} than the smart hydrogels (T_{lum}: 37.1% *vs.* 88.8%; ΔT_{sol}: 23.7% *vs.* 60.5%), which is due to the AgNW-induced strong reflection in the visible and NIR regions (Fig. S17, ESI†). Notably, the T_{lum} of 37.1% meets the building energy standard of the American Society of Heating, Refrigerating, and Air-Conditioning Engineers (ASHRAE), which recommends an assembly maximum solar heat gain coefficient of 0.21 to 0.40 for climate zones 1 to 7.[36] Fig. 4(b) illustrates a photo of the 5 cm × 5 cm durable solar/RC dual-control smart window sample at different temperatures from 15 to 45 °C and the sample gradually changes from transparent to translucent. The $\varepsilon_{Broadband}$ spectra of the smart window at 40% stretched and released states are shown
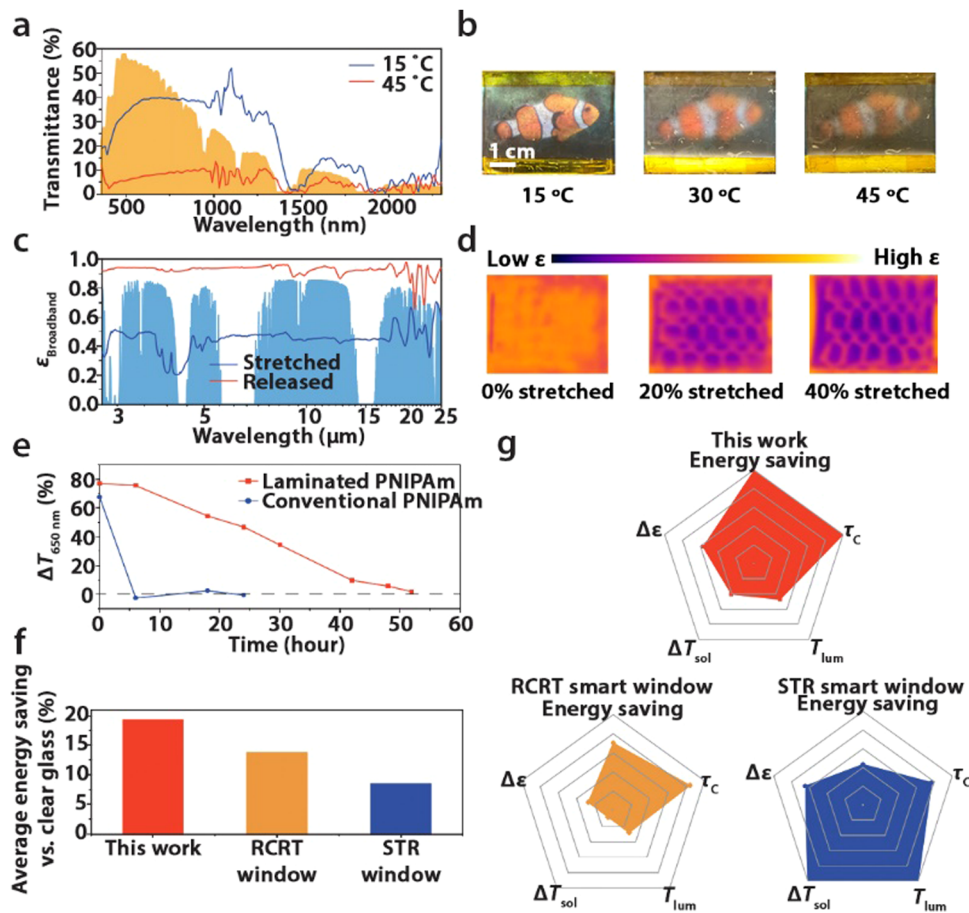
Fig. 4 (a) The UV-Vis-NIR spectra of the durable solar/RC dual-control smart window at 15 °C and 45 °C. The orange shadow represents the AM1.5 global spectrum. (b) Photos of the durable solar/RC dual-control smart window at 15, 30, and 45 °C. (c) Broadband emissivity spectra of the durable solar/RC dual-control smart window in released and stretched states. (d) IR camera images of the durable solar/RC dual-control smart window at 0%, 20%, and 40% stretching. (e) The durability test results for PNIPAm and PDMS laminated PNIPAm in the 10%RH and 25 °C environment. (f) The global average energy saving performance of the durable solar/RC dual-control smart window, RCRT smart window, and STR smart window. (g) A performance comparison of the durable solar/RC dual-control smart window and reported RCRT and STR smart windows.

in Fig. 4(c). In the released state, the sample has a high $\varepsilon_{Broadband}$ of 0.95 since its surface is fully covered by the high-E PDMS. In the 40%-stretched state, the out-of-plane structural deformation of the kirigami structure partially opens and exposes the low-E AgNWs layer underneath, resulting in a significantly decreased $\varepsilon_{Broadband}$ of 0.45. Fig. 4(d) demonstrates the switching process of $\varepsilon_{Broadband}$ *via* an IR camera, where the sample shows a gradual change from orange (high $\varepsilon_{Broadband}$) to blue (low $\varepsilon_{Broadband}$) upon stretching.

The ageing test was conducted to assess the durability of the smart window. The PNIPAm hydrogel control sample and PDMS laminated hydrogel were subjected to durability evaluation in an environment of 25 °C and humidity of 10%RH. Fig. 4(e) shows their change of transmittance at 650 nm ($\Delta T_{650 nm}$) with an increasing exposure time. It is observed that the control sample lost its optical modulation function after 6 h, while the PDMS laminated hydrogel retained its optical modulation ability for approximately 52 h, which is 9 times longer than the control sample. Furthermore, the laminated hydrogel exhibits a lifetime of 4 times longer than that of the

conventional smart hydrogel in the high-temperature durability test (Fig. S18, ESI†). The durability evaluation results demonstrate that the PDMS lamination can effectively extend the lifetime of the smart hydrogel through sealing and preventing water evaporation. We further compare the lifetime of the laminated hydrogel with that reported in the literature (Table 1) and found that it has a longer service time than conventional hydrogel preservation methods such as forming organohydrogel[37–40] or introducing ionic salt-based water absorbents.[41] Furthermore, it is worth mentioning that the introduction of an ionic salt can deactivate the smart function of hydrogels,[42] which is not preferred. The cycle stability test results of the smart window are presented in Fig. S19 (ESI†), which demonstrates that the window retains its solar modulation ability within 125 heating–cooling cycles.

A simulation of the building energy consumption was conducted to evaluate the energy-saving capability of the durable solar/RC dual-control smart window. In this simulation, an apartment model (8 m in length, 6 m in width, and 2.7 m in height) with four windows (3 m in width and 2 m in height) was

Table 1 The lifetime of recently reported long-lifetime hydrogels

Hydrogel name	Temperature (°C)	Humidity (%RH)	Lifetime (h)	Ref.
PDMS laminated hydrogel	25	10	52	This work
	60	10	24	
Glycol-poly (SBMA-co-AA) organohydrogel	25	54	9	37
Ethylene glycol-PAAm organohydrogel	60	37	10	38
PAAm-carrageenan-glycol organohydrogel	25	70	20	39
PAM/CA double network hydrogel/organohydrogel	25	50	30	40
PAAm-MgCl$_2$ hydrogel	25	10	25	41
PAAm-LiCl hydrogel	25	10	40	41

used (Fig. S20, ESI†). The windows were placed on all four sides of the building to avoid orientation bias. To assess the durable solar/RC dual-control smart window's performance, we compared its global average energy-saving performance with two other types of smart windows reported in the literature: a passive RC regulating thermochromic (RCRT) smart window[15] and a solar and thermal regulatory thermochromic (STR) smart window (Fig. 4(f)).[17] In this energy-saving performance comparison, clear glass served as the baseline and Table S3 (ESI†) presents the optical data for the clear glass and the durable solar/RC dual-control smart window utilized in the simulation. A comparison of the average energy-saving performance shows that the new design has a higher global energy-saving performance (19.2%) compared to the passive stimuli-responsive RCRT window (13.7%) and STR window (8.3%) (Fig. 4(f)). We further compare their performance in Fig. 4(g) regarding the five performance indexes of the window namely energy saving, T_{lum}, ΔT_{sol}, transition temperature (τ_c), and $\Delta\varepsilon_{Broadband}$. The durable solar/RC dual-control smart window exhibits the best energy-saving performances with a good balance of T_{lum}, ΔT_{sol}, τ_c, and $\Delta\varepsilon_{Broadband}$ among the candidates. We further conducted a 24 hours room temperature simulation for the smart window, clear glass, conventional hydrogel, and low-E glass (Fig. S21, ESI†). The results reveal that during the summer season, the room with a durable solar/RC dual-control smart window exhibits a lower temperature of ~ 2 °C in the daytime compared to the clear glass sample. Conversely, during the winter season in cold regions, the smart window demonstrates a higher room temperature than the other samples throughout the day. Overall, the newly developed durable solar/RC dual-control smart window displays a promising energy-saving performance due to its tunable solar transmittance and longwave infrared emissivity.

Conclusions

In this study, we presented a new design of a kirigami-inspired durable solar transmittance/radiative cooling dual-control smart window by integrating out-of-plane shape-morphing kirigami structures with a PDMS laminated thermal-responsive smart hydrogel. Our design has demonstrated significant improvements in durability with a nine-fold increase compared to conventional smart hydrogels such as organo-hydrogels and ionic salt-soaked hydrogels. By manipulating the geometrical features, the kirigami structure helps to maintain

the mechanical integrity of the underlying low-E layer through out-of-plane structural changes, while retaining the promising $\varepsilon_{Broadband}$ regulation ability. Through balancing T_{lum}, ΔT_{sol}, and $\Delta\varepsilon_{Broadband}$, the newly designed durable solar/RC dual-control smart window demonstrated a better energy-saving performance than the literature-reported RCRT and STR smart windows. Given its enhanced durability and promising energy-saving performance, the new smart window will inspire energy-efficient window design and construction.

Author contributions

S. Wang: investigation, formal analysis, visualization, writing – original draft; Y. Dong: investigation, formal analysis, visualization, writing – original draft; Y. Li: investigation, software, visualization, writing – original fraft; K. Ryu: visualization; Z. Dong: supervision, writing – review & editing; J. Chen: investigation; Y. Ke: validation, writing – review & editing; Z. Dai: supervision, writing – review & editing; J. Yin: supervision, software, writing – review & editing; and Y. Long: conceptualization, funding acquisition, project administration, supervision, writing – review & editing.

Conflicts of interest

There are no conflicts to declare.

Acknowledgements

References

1 U. Berardi, *Resour., Conserv. Recycl.*, 2017, **123**, 230–241.
2 L. Zhao, X. Lee, R. B. Smith and K. Oleson, *Nature*, 2014, **511**, 216.
3 Y. Gao, S. Wang, L. Kang, Z. Chen, J. Du, X. Liu, H. Luo and M. Kanehira, *Energy Environ. Sci.*, 2012, **5**, 8234–8237.
4 E. S. Lee, X. Pang, S. Hoffmann, H. Goudey and A. Thanachareonkit, An empirical study of a full-scale polymer thermochromic window and its implications on material

science development objectives, Report 0927-0248, Lawrence Berkeley National Laboratory, 2013.

5 Z. Shao, A. Huang, C. Ming, J. Bell, P. Yu, Y.-Y. Sun, L. Jin, L. Ma, H. Luo, P. Jin and X. Cao, *Nat. Electron.*, 2022, **5**, 45–52.

6 R. Li, X. Ma, J. Li, J. Cao, H. Gao, T. Li, X. Zhang, L. Wang, Q. Zhang, G. Wang, C. Hou, Y. Li, T. Palacios, Y. Lin, H. Wang and X. Ling, *Nat. Commun.*, 2021, **12**, 1587.

7 Y. Zhou, S. Wang, J. Peng, Y. Tan, C. Li, F. Y. C. Boey and Y. Long, *Joule*, 2020, **4**, 2458–2474.

8 Q. Zhang, Y. Jiang, L. Chen, W. Chen, J. Li, Y. Cai, C. Ma, W. Xu, Y. Lu, X. Jia and Z. Bao, *Adv. Funct. Mater.*, 2021, **31**, 2100686.

9 A. Kanwat, B. Ghosh, S. E. Ng, P. J. S. Rana, Y. Lekina, T. J. N. Hooper, N. Yantara, M. Kovalev, B. Chaudhary, P. Kajal, B. Febriansyah, Q. Y. Tan, M. Klein, Z. X. Shen, J. W. Ager, S. G. Mhaisalkar and N. Mathews, *ACS Nano*, 2022, **16**, 2942–2952.

10 S. Y. Chun, S. Park, S. I. Lee, H. D. Nguyen, K.-K. Lee, S. Hong, C.-H. Han, M. Cho, H.-K. Choi and K. Kwak, *Nano Energy*, 2021, **82**, 105721.

11 Y. Zhou, F. Fan, Y. Liu, S. Zhao, Q. Xu, S. Wang, D. Luo and Y. Long, *Nano Energy*, 2021, **90**, 106613.

12 H. Chen, D. Cho, K. Ko, C. Qin, M. P. Kim, H. Zhang, J.-H. Lee, E. Kim, D. Park, X. Shen, J. Yang, H. Ko, J.-W. Hong, J.-K. Kim and S. Jeon, *ACS Nano*, 2022, **16**, 68–77.

13 X. Yin, R. Yang, G. Tan and S. Fan, *Science*, 2020, **370**, 786–791.

14 A. P. Raman, M. A. Anoma, L. Zhu, E. Rephaeli and S. Fan, *Nature*, 2014, **515**, 540.

15 S. Wang, T. Jiang, Y. Meng, R. Yang, G. Tan and Y. Long, *Science*, 2021, **374**, 1501–1504.

16 K. Tang, K. Dong, J. Li, M. P. Gordon, F. G. Reichertz, H. Kim, Y. Rho, Q. Wang, C.-Y. Lin, C. P. Grigoropoulos, A. Javey, J. J. Urban, J. Yao, R. Levinson and J. Wu, *Science*, 2021, **374**, 1504–1509.

17 C. Lin, J. Hur, C. Y. H. Chao, G. Liu, S. Yao, W. Li and B. Huang, *Sci. Adv.*, 2022, **8**, eabn7359.

18 Y. Rao, J. Dai, C. Sui, Y.-T. Lai, Z. Li, H. Fang, X. Li, W. Li and P.-C. Hsu, *ACS Energy Lett.*, 2021, **6**, 3906–3915.

19 Z. Zhou, Y. Fang, X. Wang, E. Yang, R. Liu, X. Zhou, Z. Huang, H. Yin, J. Zhou and B. Hu, *Nano Energy*, 2022, **93**, 106865.

20 S. Wang, Y. Zhou, T. Jiang, R. Yang, G. Tan and Y. Long, *Nano Energy*, 2021, **89**, 106440.

21 Y. Y. Cui, Y. Ke, C. Liu, N. Wang, Z. Chen, L. M. Zhang, Y. Zhou, S. Wang, Y. F. Gao and Y. Long, *Joule*, 2018, **2**, 1707–1746.

22 Y.-X. Ji, S.-Y. Li, G. A. Niklasson and C. G. Granqvist, *Thin Solid Films*, 2014, **562**, 568–573.

23 T. Chang, X. Cao, N. Li, S. Long, Y. Zhu, J. Huang, H. Luo and P. Jin, *Matter*, 2019, **1**, 734–744.

24 C. Cao, B. Hu, G. Tu, X. Ji, Z. Li, F. Xu, T. Chang, P. Jin and X. Cao, *ACS Appl. Mater. Interfaces*, 2022, **14**, 28105–28113.

25 X. Zhou, Y. Meng, T. D. Vu, D. Gu, Y. Jiang, Q. Mu, Y. Li, B. Yao, Z. Dong, Q. Liu and Y. Long, *J. Mater. Chem. A*, 2021, **9**, 15618–15628.

26 Y. Yu, P. Yi, W. Xu, X. Sun, G. Deng, X. Liu, J. Shui and R. Yu, *Nano-Micro Lett.*, 2022, **14**, 77.

27 Z. Han, P. Wang, Y. Lu, Z. Jia, S. Qu and W. Yang, *Sci. Adv.*, 2022, **8**, eabl5066.

28 S. Zhang, S. Cao, T. Zhang, Q. Yao, A. Fisher and J. Y. Lee, *Mater. Horiz.*, 2018, **5**, 291–297.

29 G. Cai, J. Chen, J. Xiong, A. Lee-Sie Eh, J. Wang, M. Higuchi and P. S. Lee, *ACS Energy Lett.*, 2020, **5**, 1159–1166.

30 H. Fu, X. Hong, A. Wan, J. D. Batteas and D. E. Bergbreiter, *ACS Appl. Mater. Interfaces*, 2010, **2**, 452–458.

31 T. Munk, S. Baldursdottir, S. Hietala, T. Rades, M. Nuopponen, K. Kalliomäki, H. Tenhu, J. Rantanen and C. J. Strachan, *Polymer*, 2013, **54**, 6947–6953.

32 X.-H. Li, C. Liu, S.-P. Feng and N. X. Fang, *Joule*, 2019, **3**, 290–302.

33 Y. Ke, Y. Yin, Q. Zhang, Y. Tan, P. Hu, S. Wang, Y. Tang, Y. Zhou, X. Wen, S. Wu, T. J. White, J. Yin, J. Peng, Q. Xiong, D. Zhao and Y. Long, *Joule*, 2019, **3**, 858–871.

34 Y. Tang, G. Lin, S. Yang, Y. K. Yi, R. D. Kamien and J. Yin, *Adv. Mater.*, 2017, **29**, 1604262.

35 T. C. Shyu, P. F. Damasceno, P. M. Dodd, A. Lamoureux, L. Xu, M. Shlian, M. Shtein, S. C. Glotzer and N. A. Kotov, *Nat. Mater.*, 2015, **14**, 785–789.

36 ANSI/ASHRAE/IES, Energy standard for building except low-rise residential buildings, 2019.

37 X. Sui, H. Guo, C. Cai, Q. Li, C. Wen, X. Zhang, X. Wang, J. Yang and L. Zhang, *Chem. Eng. J.*, 2021, **419**, 129478.

38 J. Wu, Z. Wu, H. Xu, Q. Wu, C. Liu, B.-R. Yang, X. Gui, X. Xie, K. Tao, Y. Shen, J. Miao and L. K. Norford, *Mater. Horiz.*, 2019, **6**, 595–603.

39 J. Wu, Z. Wu, S. Han, B.-R. Yang, X. Gui, K. Tao, C. Liu, J. Miao and L. K. Norford, *ACS Appl. Mater. Interfaces*, 2019, **11**, 2364–2373.

40 Y. Wei, H. Wang, Q. Ding, Z. Wu, H. Zhang, K. Tao, X. Xie and J. Wu, *Mater. Horiz.*, 2022, **9**, 1921–1934.

41 Y. Bai, B. Chen, F. Xiang, J. Zhou, H. Wang and Z. Suo, *Appl. Phys. Lett.*, 2014, **105**, 151903.

42 Y. Zhou, C. Wan, Y. Yang, H. Yang, S. Wang, Z. Dai, K. Ji, H. Jiang, X. Chen and Y. Long, *Adv. Funct. Mater.*, 2019, **29**, 1806220.